



HAL
open science

Influence of Ga + milling on the spin waves modes in a Co₂MnSi Heusler magnonic crystal

S. Manton, Nicolas Biziere

► **To cite this version:**

S. Manton, Nicolas Biziere. Influence of Ga + milling on the spin waves modes in a Co₂MnSi Heusler magnonic crystal. *Journal of Applied Physics*, 2022, 131 (11), pp.113905. 10.1063/5.0085623. hal-03620920

HAL Id: hal-03620920

<https://hal.science/hal-03620920>

Submitted on 27 Mar 2022

HAL is a multi-disciplinary open access archive for the deposit and dissemination of scientific research documents, whether they are published or not. The documents may come from teaching and research institutions in France or abroad, or from public or private research centers.

L'archive ouverte pluridisciplinaire **HAL**, est destinée au dépôt et à la diffusion de documents scientifiques de niveau recherche, publiés ou non, émanant des établissements d'enseignement et de recherche français ou étrangers, des laboratoires publics ou privés.

Influence of Ga⁺ milling on the spin waves modes in a Co₂MnSi Heusler magnonic crystal.

S. Manton and N. Biziere

CEMES, Université de Toulouse, CNRS, UPS, 29 rue Jeanne Marvig, F-31055 Toulouse, France

Corresponding author : N. Biziere
e.mail : nicolas.biziere@cemes.fr

Abstract: Ferromagnetic resonance experiment was performed to study the magnonic modes of an antidot lattice nanopatterned in a sputtered Co₂MnSi Heusler alloy thin film. The magnonic crystal was prepared with Ga⁺ focused ion beam and micromagnetic simulations were used to explain qualitatively and quantitatively the complex experimental spin waves spectrum. We demonstrate the necessity to consider the geometrical imperfections and the modification of the Co₂MnSi magnetic parameters induced by the nanofabrication process to describe the evolution of the frequencies and spatial profiles of the principal experimental spin waves modes in the 0 - 300 mT magnetic field range. In particular, our model suggests that Ga⁺ milling induces a drastic decrease (between 80 and 90 %) of the bulk Co₂MnSi magnetic parameters. In addition, simulations reveal the presence of a diversity of localised and extended spin wave modes whose spatial profiles are closely related to the evolution of the magnetic state at equilibrium from a very non-collinear configuration up to a quasi-saturated state.

I. Introduction.

Magnonic crystals (MC) are magnetic metamaterials where the magnetic properties are artificially and periodically modulated. This new class of materials offers many attractive opportunities in the field of microwave to Terahertz devices. Indeed, in analogy to photonic crystals with electromagnetic waves, spin waves propagating in such periodic structures are subject to Bragg scattering resulting in the formation of frequency band-gaps in the spin waves dispersion relation. Due to the small wavelengths of spin waves in magnetic materials (from μm to nm), they offer interesting features to reduce the dimensions of microwave devices and on chip integration. Then, many applications have been proposed such as data computing¹ or ² for example. In addition, MC are also very interesting to make passive microwave devices such as filters operating at zero field offering reconfigurable magnetic states to obtain on demand various microwave absorption spectra. Such systems, called reconfigurable magnonic devices, have become the topic of intense research in the past few years³⁻⁷.

Materials used for fundamental studies on MC and more generally in magnonics are generally Yttrium iron garnet (YIG) and Permalloy (NiFe). YIG is an insulator and has the lower dynamic damping coefficient among magnetic material ($2 \cdot 10^{-4}$). This allows propagating spin waves over long distances, up to the millimetre range in the case of μm -thick YIG films¹. However, it has a low saturation magnetization that limits high frequency (few GHz) applications. On the contrary, Permalloy is a metal and is widely used due to its easiness of fabrication/deposition and

nanostructuring, its relatively high saturation magnetization and its low damping ($6 \cdot 10^{-3}$). Nevertheless, the distance over which spin waves propagates is far shorter, of the order of few μm only.

Heusler alloys with general formula Co₂YZ offer an interesting alternative to these materials. For example Co₂MnSi (CMS) offers high Curie temperature (around 985 K⁸), a low spin wave damping down to $7 \cdot 10^{-4}$ for long spin waves propagation distances⁹⁻¹¹. It also presents a high saturation magnetization (1.26 T)^{12,13} which allows operating with frequencies above the GHz range at remanence and could result in larger frequency band gaps in MC^{14,15}. It also presents a high spin polarization (above 90% experimentally)¹⁶⁻²¹ allowing interesting magnon spintronic devices²²⁻²⁴. However, to our knowledge, only few magnonics studies^{10,11,25-28} have been performed up to now with such materials and few Co-based Heusler alloy magnonic crystals exist in the literature^{29,30}.

Besides the choice of material, several strategies have been proposed to modulate the magnetic properties in MC by varying different parameters such as the geometry (dots and antidots³¹⁻³⁵, thickness³⁶ or width modulation in thin films³⁷), the magnetic constants (bi-component^{38,39} or ion implanted structures⁴⁰) or the applied magnetic field³. In particular, magnetic antidot lattices (MAL) allow the exploration of various devices applications such as ultra-high density magnetic data storage media^{41,42}, filters and waveguides^{34,43,44} and sensors⁴⁵.

Different nanostructuring techniques have been used to fabricate MAL. The main ones are e-beam lithography and lift-off processes, combination of e-

beam lithography and ion milling^{29,46}, deep ultraviolet lithography and lift-off^{33,47}, Focused Ion Beam (FIB)⁴⁸⁻⁵¹ or template synthesis in porous membranes⁵². Among them, Ga⁺ FIB milling is widely used because it is a fast direct writing technique into a magnetic thin film. However, it is known in microelectronic that possible drawbacks of Ga⁺ milling are ion implantation, chemical mixing⁵³⁻⁵⁹ etc. While different MAL fabricated by FIB were studied in the literature, there are generally no considerations about the effects of Ga⁺ ion implantation or local edge roughness induced by milling processes on the spin waves properties in the particular context of magnonic studies. In particular, micromagnetic simulations are generally performed in ideal geometries, neglecting geometrical or magnetic defects. This can explain some discrepancies observed in the spin wave frequencies between numerical studies and experiments^{32,49,60}. Such discrepancies are even more pronounced at remanence or at low magnetic fields because the equilibrium state, defining the spin waves spectrum, strongly varies with the local geometrical and magnetic imperfections. Consequently, agreements between numerical studies and experiments are generally achieved only qualitatively and in the magnetic saturated state regime but not on a large field range.

In this article, we address the impact of Ga⁺ FIB milling on CMS Heusler alloy to make a micrometer sized 2D lattice of antidots arranged in a cubic lattice. Such simple geometry allow working on a model system which have been studied in many other MAL. While FIB milling can have a small impact on the magnetic properties of materials such as permalloy, its influence on Heusler alloys has been poorly discussed in the literature⁶¹. For this, we measured the spin waves spectrum of the MC by ferromagnetic resonance (FMR) experiments in the field range (0 – 300 mT). The results are compared to numerical simulations of the field evolution of the static and dynamic magnetic states. A quantitative agreement with the experiment in the full field range is obtained with a simplified micromagnetic model considering the particular shape of the antidots induced by the milling, in addition to an impacted volume of few tens of nanometers around the holes with strongly reduced magnetic parameters.

II. Experimental and numerical methods.

An epitaxial thin film of CMS was grown on a MgO (001) single crystal substrate by ultrahigh vacuum magnetron sputtering with a base pressure of $4 \cdot 10^{-8}$ mbar. The deposition conditions are the same as presented in⁶² except that the annealing of the CMS thin film was done at 700°C for 2h. This deposition procedure favours the L2₁ phase ordering of CMS leading to a high magneto crystalline anisotropy field and a low magnetic damping^{12,63}. The expected thickness of the layer is 50 nm.

We have measured the magnetic parameters on another thin film grown in similar conditions. The magnetic parameters obtained are $\mu_0 M_s = 1.29 \pm 0.01$ T, the cubic anisotropy constant $K_c = 16.9 \pm 0.05 \cdot 10^3$ J/m³, the exchange constant $A = 19 \pm 0.05 \cdot 10^{-12}$ J/m, $\gamma = 28.7 \pm 0.1$ GHz/T, and the Gilbert damping coefficient $\alpha = 2 \pm 0.5 \cdot 10^{-3}$. These magnetic parameters are very close from the ones obtained in our previous experimental results on Co₂MnSi alloys¹² or obtained by others⁶³.

The antidot lattice was patterned by Ga⁺ Focused Ion Beam (FIB) milling with a Helios dual beam FIB-SEM. The borders of the square lattice are parallel to the two magnetic easy axes of the Co₂MnSi thin film. The high voltage used was 30 keV with a beam current of 73 pA. An example of such MC is shown in Fig. 1(a). This image was obtained for an antidot lattice made in the same conditions as the one for the FMR experiments and from the same thin film. The lattice covers an area of $45 \times 45 \mu\text{m}^2$ with square antidots of nominal size and spacing 100 nm and 300 nm respectively. The thickness of the CMS measured on a cross section of the antidots is 50 ± 5 nm (Fig. 1.(c)) and the total depth of the hole is about 200 nm. This cross section also highlights the complexity of the etched structures, as the size of the antidots is larger at the top than at the bottom leading to a bowl geometry. Similar shapes were observed by others⁶⁴. This is confirmed with SEM images obtained at a tilted angle of 52° (Fig. 1(b)).

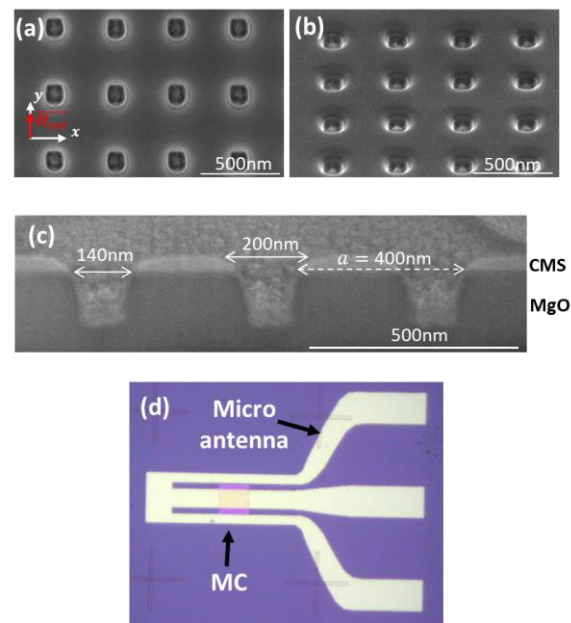


FIG. 1. (a) SEM image of the antidot lattice. (b) Tilted SEM image (52°) of the antidot lattice. (c) Cross section of the antidot lattice. (d) Optical image of the micro-antenna on top of the magnonic crystal.

A more detailed analysis reveals a complex geometry where the holes at the bottom of the film have a square shape with rounded edges while they present

a circular shape at the top. The dimensions of the holes are $200 \text{ nm} \pm 20 \text{ nm}$ at the top and $140 \text{ nm} \pm 10 \text{ nm}$ at the bottom. The separation from center to center between two holes is 400 nm . Such complex geometry is induced by the conical shape of the ionic beam related to the focalization of the spot convoluted with the Gaussian distribution of the spot intensity. In our case, the measured apparent beam spot size is approximately 60 nm , larger than the theoretical 20 nm diameter calculated for this ionic current.

Once the antidot lattice is obtained, a short-ended coplanar waveguide (CPW) acting as a micro antenna for FMR measurements is made by laser lithography and lift-off of 10 nm of Ti and 150 nm of Au. The width of the inner and outer conductors are 30 and $15 \mu\text{m}$ respectively and the gap is $10 \mu\text{m}$. The large central conductor ensures a quasi-uniform pumping field on the surface of the array (Fig 1(d)). The micro antenna is electrically isolated from the metallic CMS layer by a 200 nm thick Si_3N_4 passivation layer.

Broadband FMR experiments was performed to measure the evolution of the resonance frequencies as a function of the external magnetic field H_0 . The sample is placed in an electromagnet providing a static magnetic field up to 300 mT . The coplanar waveguide is connected with a picoprobe to a microwave Agilent ($0.1\text{-}30\text{GHz}$). The reflected microwave signal from the antenna passes through a circulator and a microwave diode connected to an Ametek lock-in amplifier. This allows measuring the microwave power absorbed by the sample at resonance. For this, H_0 is modulated with an amplitude of 0.2 mT at a frequency of 113 Hz as in ¹². Measurements are performed at a fixed microwave frequency while H_0 is swept from a strong value of 300 mT , that can saturate the sample, down to 0 mT .

To explain the experimental measurements, micromagnetic simulations were performed with Mumax ⁶⁵ to calculate the static and dynamic states of the antidot array. We simulated a unit cell as shown in Fig. 2. As discussed in section III, we have tested different geometries of antidots. The geometries are shown in Figs. 2(a) and (b). We always kept the distance between the centers of the antidots equal to 400 nm , i.e. the nominal expected spacing. The lateral dimensions of the squares and the diameter of the circles are 140 nm . Rounded squares are obtained by considering the intersection between a square with lateral sizes 140 nm with a 160 nm diameter circle. For the bowl shape, which is the closest geometry to the one observed in the SEM images of Fig. 1, we applied the following method. We consider at the bottom of the antidot lattice a square with rounded angles as defined above. Then, the geometry turns into circular holes with increasing diameters up to 200 nm when going up to the top of the layer. The geometry obtained is shown in Figs. 2(b) and (c).

The dimensions of the unit cell is $800 \times 800 \times 50 \text{ nm}^3$ while the full volume for the simulation is $800 \times 800 \times 70 \text{ nm}^3$. The system was discretized with rectangular cells of dimensions $5 \times 5 \times 5 \text{ nm}^3$ below the

exchange length of the CMS ($\approx 5.4 \text{ nm}$). We obtained the same results for dimensions of the cells of $2.5 \times 2.5 \times 2.5 \text{ nm}^3$ but this implies large computer resources. 2D Periodic boundary conditions (PBC) are used to reproduce an infinite 2D lattice and perform numerous tests with reasonable simulation times. However, we verified that our results presented in section III and IV are the same for a finite system with lateral dimensions $40 \times 40 \mu\text{m}^2$ and with a microwave excitation over a width of $30 \mu\text{m}$ to mimic the experiment. Such large simulations require important computer resources and have been performed with OOMMF on the HPC resource of Calmip supercomputing center. We observed no difference on the spin waves frequencies for a system with 2D PBC on Mumax 3 and for the finite dimensions system on OOMMF.

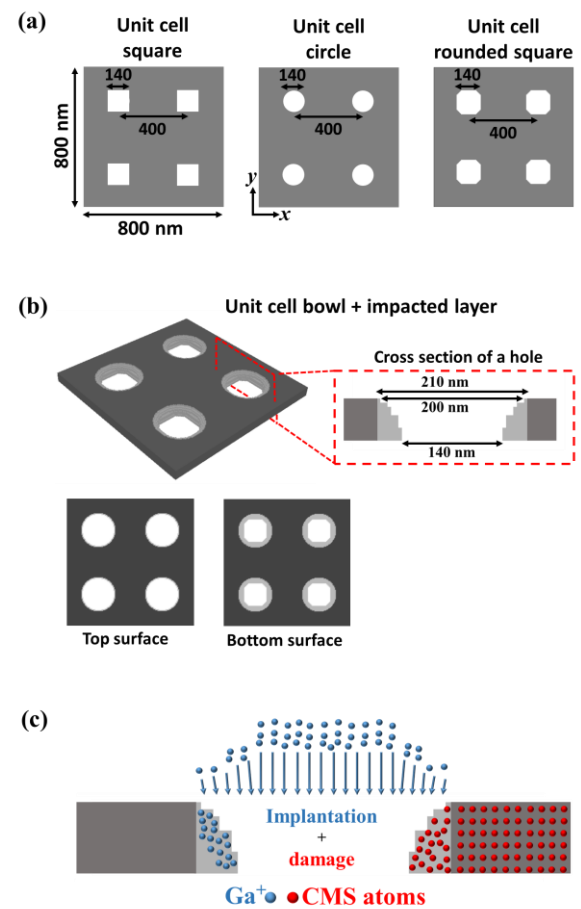


FIG. 2. Scheme of the unit cell used for micromagnetic simulations. The antidots (here in white) can have square, circle or rounded square shapes as explained in the text. (b) Bowl geometry with the volume around the holes impacted by the milling highlighted in light grey. (c) Schematic of the Ga^+ implantation and lateral damage induced by the milling around the holes. Only one process is shown on each side of the hole for clarity.

The material parameters used in the simulations are $\gamma = 28.7 \text{ GHz/T}$, $\mu_0 M_S = 1.29 \text{ T}$, $A =$

19.10^{-12} J/m, $K_c = 17.10^3$ J/m³ and $\alpha = 1.10^{-3}$. The low damping coefficient used in the simulations allow getting well-resolved spin waves modes in the calculated FFT spectrum. The magnetization easy axes due to the cubic anisotropy are parallel to the x and y directions.

To calculate the magnetic equilibrium states for different values of H_0 , we start with a random distribution of the magnetization in the different cells. Then, we apply a 1 T saturation field along the y axis, with a slight deviation of 5° . This angle has been estimated experimentally and is due to a misalignment of the applied field with the edge of the magnonic crystal when we set our sample holder in the electromagnet. The system is relaxed to its equilibrium magnetization in 100 mT steps from 1 T to 500 mT and in 10 mT steps from 500 mT to 0 mT. Once the equilibrium is reached, a magnetic pulse h_{rf} in the form of a temporal *Sinc* function is applied in the x direction to excite SW modes over a broad frequency range⁶⁶. The cutting frequency of the *Sinc* pulse is 30 GHz. The amplitude of h_{rf} is 2 mT, ensuring to be in the linear regime of spin waves excitation, and is uniform over the entire unit cell.

To reproduce qualitatively the amplitude of the signals measured by the micro-antenna associated to the different spin waves modes, we record the temporal evolution of the z component of the stray field $h_{d,z}(t)$ in the plane located at 10 nm above the top surface of the magnonic crystal. Indeed, in micro-antenna measurements, the variation of impedance at the origin of the reflected microwave power is related to the inductive voltage generated by the out of plane component of the magnetic induction through the Lenz-Faraday law. The value of $h_{d,z}(t)$ is averaged over all the cells of the plane. We record 4096 values of $h_{d,z}(t)$ every 10 ps. To obtain the spin waves frequency spectrum, we apply a temporal FFT. Let's note that all frequency values were confirmed by doing the same numerical treatment on the $M_z(t)$ value averaged over all cells in the MC.

In order to obtain the spatial profile of the different spin waves modes, we also record 4096 files every 10 ps of the M_x component for every cell in the top surface plane of the MC. We subtract the equilibrium magnetic state to each file in order to keep only the dynamic $m_x(t)$ component. Then, the spin wave spatial profile at a particular frequency is recovered via a FFT transformation performed on the temporal evolution of m_x in every cell, followed by an IFFT at the frequency of interest. The final images discussed in section IV correspond to the temporal snapshots at which $m_x(t)$ in the central cell of the plane is maximum.

III. FMR measurements and simulations results.

Fig. 3 presents the FMR measurements showing the evolution of the microwave absorption spectrum as a function of the applied field $f(H_0)$. The

amplitude of the recorded FMR signal is color coded with the color code shown on the left of the figure. As a general observation, the spectrum appears to be quite large in frequency, meaning a large broadening of the different principal spin waves modes. These modes are shown by arrows in the inset at the top of Fig. 3 corresponding to the measured lock-in signal at 9.5 GHz. The principal modes are also highlighted in the figure with colored symbols at particular fields obtained from micromagnetic simulations as discussed below. In the inset, the most intense mode at low field shows the smallest peak-to-peak linewidth (≈ 2 mT) while other modes show linewidths of few mT (up to 13 mT) explaining their relatively small intensity.

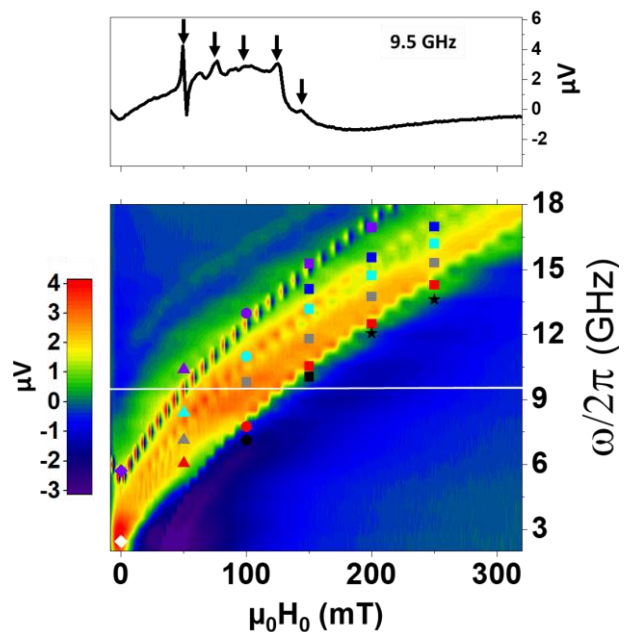


FIG. 3. Evolution of the microwave power absorbed by the antidot lattice as a function of the applied field H_0 and microwave frequency. The amplitude of the signal is color coded following the color bar on the left. At the top, example of FMR spectrum recorded at 9.5 GHz (white line in the main figure) showing the main resonance peaks. The colored symbols correspond to the simulated spin waves modes at different applied fields described in section IV. The colored symbols are the same as in Fig. 5.b.

To reproduce the spin waves spectrum properties of Fig. 3, we first discuss the importance of the geometry of the holes without considering possible variations of the magnetic parameters induced by Ga^+ milling. Geometrical variations are often assumed in literature to explain the discrepancies between numerical and experimental data. However, to our knowledge, it is rarely demonstrated and quantified^{67,68}.

As an example, we show in Fig. 4(a) the FFT spectra obtained at $H_0 = 200$ mT for different geometries such as perfect squares, circles, squares with rounded angles, or bowl shapes. We observe that

each shape leads to several principal spin waves modes. The frequency range at which the simulated modes appear is in good agreement with the frequencies of the measured resonance peaks. The number in the image corresponds to the spin waves modes with similar spatial profile. One can see that the frequency and amplitude of the different modes depend strongly on the antidot shape. This is particularly pronounced for the mode 1 where the discrepancy between the square and circle shape can be as high as 1.5 GHz. The frequency of the mode 2 for the square, circle and rounded square shapes are close to each other but it is 1 GHz lower in the bowl shape.

Therefore, we assume that small local variations of shape and dimension occurring from one antidot to the other across the sample are probably one of the main cause of the large linewidth of the experimental resonance peaks. Indeed, experiments are performed at a fixed frequency while sweeping the magnetic field. Then, the local variation of shapes induce small variations of the resonance fields across the sample, broadening the peaks linewidths. We also observe in the calculated FFT spectrum the presence of small satellite peaks around the main modes (modes 2 and 3 for example). If the damping coefficient is increased up to $5 \cdot 10^{-3}$, the satellite peaks collapse with the main modes leading to a broadening of those ones (not shown here). As will be shown below, the introduction of a volume around the holes with modified magnetic parameters tends to smooth the satellite peaks (Fig. 4(b)).

One of the main conclusions of our FFT calculations is that the most intense experimental mode observed in Fig. 3 (around 17 GHz at $H_0 = 200$ mT) could not be reproduced satisfactorily in the numerical simulations, neither in frequency nor in amplitude even considering the different geometries. This includes the bowl shape with dimensions and geometry as close as possible as the one deduced from SEM observations. To explain such discrepancies, we have to consider the local modifications of the CMS magnetic properties induced by the Ga^+ milling.

FIB milling induces a volume around the holes where the magnetic properties of the CMS alloy are impacted. First, it is responsible for lateral damages. Indeed, each incoming ion induces multiple collisions events in the CMS atoms that can lead to Frenkel pairs and vacancies creation. Such kind of effects have been observed for high energy He^+ irradiation in CMS thin film^{12,13}. The second effect is related to the Ga^+ ion implantation around the holes that induces further collisions with the CMS atoms and a modification of the local electronic structure of the CMS. Let's note that damage and implantation are cumulative processes, meaning that they increase with the ion fluence (i.e. the number of ions/cm²).

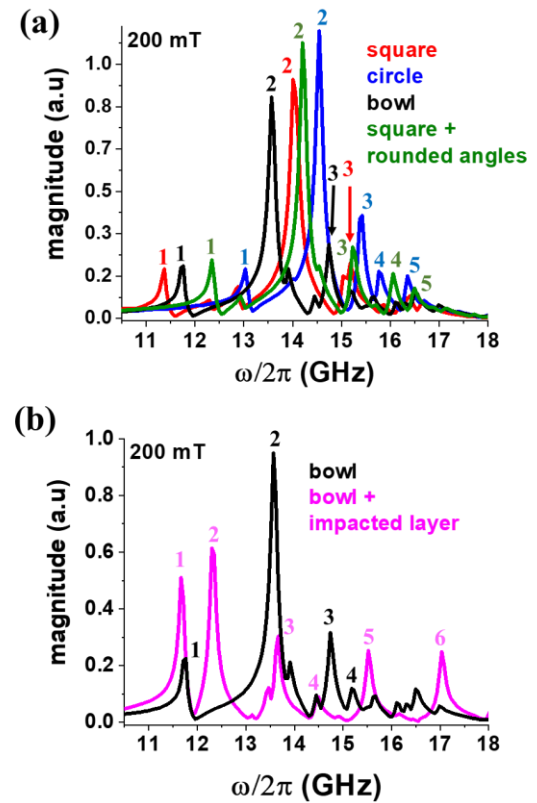


FIG. 4. (a) FFT spectrum for different antidots shapes at $H_0 = 200$ mT. (b) FFT spectrum of a bowl shape with and without an impacted volume on the edge of the antidot at $H_0 = 200$ mT and $\beta = 10$. For the bowl shape with impacted volume, the mode numbers correspond to the mode numbers in Fig. 5.

The distances over which implantation and lateral damage spread are material dependent⁶⁹. To evaluate them, we performed SRIM (Stopping and Range of Ions in Matter) simulations⁷⁰. The density of the CMS alloy is $8.85 \cdot 10^{22}$ at/cm³ (7.396 g/cm³) and the atoms are randomly distributed. At 30 keV, the stopping range of Ga^+ ions inside the CMS is 30 nm and the lateral damage is 20 nm all around the trajectory of the incoming ions. The latter is roughly equivalent to the difference of radius between the top and the bottom of the hole. It is most probable that the lateral damage and ion implantation gradually change when going from the edge of the hole toward the bulk CMS and from the bottom to the top surface, as schematically depicted in Fig. 2(c). However, considering that the impacted volume is a complex mixture of damaged CMS atoms and implanted Ga^+ ions, we adopted a simplified approach assuming a uniform volume around the holes where the magnetic parameters of the CMS are modified. This volume is obtained as the intersection of a simple 210 nm diameter cylinder with the bowl shape of the antidot. This impacted layer is shown in light grey in the Figs. 2(b) and (c).

Now, the next step is to define the variations of magnetic parameters in the impacted volume. The main problem is the lack of information in literature for the interaction between Ga^+ ions and Heusler alloys. In general, for ferromagnetic metals, it is known that Ga^+ irradiation may affect the magnetic properties of thin films through a reduced saturation magnetization, exchange interactions and magneto crystalline anisotropy^{61,71–74}. Many different mechanisms such as amorphization, modifications of local electronic properties due to ion implantation, chemical mixing or vacancy generation^{75–77} can be at the origin of these magnetic variations. Recently, Ga^+ ion milling was assumed to be the reason for the apparition of unexpected localized spin waves modes in magnetic antidots patterned in Co/Pd multilayers⁷¹. Such modes are shown to originate from a local decrease of the perpendicular magneto crystalline anisotropy around the antidots leading to a rotation of the magnetization in the plane of the sample. However, no modification of the other parameters (such as M_s for example) is discussed in this work.

To our knowledge, only the work of Hamrle et al.⁶¹ addresses the question of the impact of Ga^+ ions at 30 keV on the magnetic properties of a ultra-thin (11 nm) Co_2FeSi Heusler film. This material is quite similar to Co_2MnSi . They demonstrate a gradual transition from a ferromagnetic to paramagnetic state in the alloy, with a fully paramagnetic state obtained for a fluence around $9 \cdot 10^{16}$ ions/cm². Also, they observe a reduction of the exchange constant for fluences in the range of 10^{15} ions/cm² while first order spin-orbit coupling (at the origin of cubic anisotropy) is found to decrease for a fluence as low as 10^{14} ions/cm². Therefore, they observe already some effects at moderate fluences.

To compare their experiment with our, we have estimated the fluence of Ga^+ ions in the tail of our beam spot, so roughly in the impacted volume. Considering only 10% of ions in the tail of the beam and with our experimental conditions, it is estimated between 10^{18} to 10^{19} ions/cm². This value is higher than the one studied by Hamrle et al. Consequently, we assume a very strong reduction of the magnetic parameters of CMS in our experiment. In the micromagnetic simulations we made the simple assumption that the milling process equally modified them in the impacted volume. More precisely, M_s , A , H_k , are divided by a factor β with respect to their bulk values while the damping coefficient is multiplied by β . Then, we varied β until we obtained a qualitative and quantitative agreement between the numerical calculated spin waves frequencies and FMR measurements.

The Fig. 4(b) shows an example of an FFT spectrum calculated at $H_0 = 200$ mT for $\beta = 10$ where the consequence of the impacted volume is clearly observed. For such value of β , we can consider that the layer around the hole is almost paramagnetic but not completely. A general observation when comparing the

spin waves frequencies for the bowl shape with or without the impacted layer, is the shift to lower frequencies when we have the impacted layer, except for the first mode. As a rough approximation, this is because the impacted layer acts almost as vacuum and reduces artificially the distance between the holes. This leads to the increase of the demagnetizing field amplitude between the antidots (in the $-y$ direction) and a decrease of the effective field (in the $+y$ direction)⁷⁸. Finally, one of the most important consequence is the appearance of a quite intense mode at 17 GHz (mode 6), in good agreement with the experimental data. Let's note that the position of the modes 1 and 2 are more sensitive to local variations of geometries than the mode 6 for example. This is in agreement with the larger experimental broadening of these peaks and explain why the highest frequency mode appears to be the most intense experimentally.

The simulated modes for $\beta = 10$ at different values of H_0 are shown by the colored symbols in the Fig. 3. Their spatial profile is discussed in the next section. One can see the very good agreement over the entire field range. We also performed simulations (not shown here) considering that the impacted volume is completely non-magnetic. Surprisingly, in this particular case, simulations do not fit adequately the experimental spectrum, especially at 0 and 50 mT, for which the disagreement between the experimental spectrum and the lowest frequency modes can be as high as 1.5 GHz. Considering as a starting point that all magnetic parameters reduce similarly, an agreement with the experimental data have been found satisfactory for β between 5 and 10, with the best agreement for $\beta = 10$. However, it might be possible to find other combinations of reduced magnetic parameters that could fit the experimental data⁷⁹. This requires further studies of the influence of Ga^+ implantation to find the dependency of M_s , A and H_k with the ion fluence. Nevertheless, even if our model is simplified and further refinements might be necessary, it tends to demonstrate a strong reduction of the magnetic parameters but without reaching a full paramagnetic state. More importantly, it also clearly demonstrates the importance of considering both the geometry and the modifications of the magnetic parameters in the impacted volume nearby the antidots to fully describe the spin waves spectrum in the entire field range.

IV. Evolution of spin waves profiles with the applied field.

To go further in our analysis, we now discuss the evolution of the equilibrium magnetic states and spatial profile of the different spin waves modes simulated with the impacted layer ($\beta = 10$). We start with the study of the equilibrium magnetization configuration at different values of H_0 (0, 50, 100, 150, 200 and 250 mT) applied at 5° from the y axis. Fig. 5(a) shows the magnetic configurations in the top surface

This is the author's peer reviewed, accepted manuscript. However, the online version of record will be different from this version once it has been copyedited and typeset.
PLEASE CITE THIS ARTICLE AS DOI: 10.1063/1.50085623

plane of the MC. The color code corresponds to the amplitude of the M_x component.

The equilibrium configuration strongly varies with the amplitude of H_0 . At 0 mT (remanence), the magnetization is parallel to the x direction in the area between vertical antidots while it is aligned along y between horizontal antidots. In the central part of the unit cell, a domain with the magnetization rotated at about 45° from the x axis appears. When increasing H_0 , the magnetization between vertical and horizontal antidots begins to rotate toward the direction of the applied field but we can observe that the domain in the center of the unit cell remains for field values up to 50 mT. It is only for field values above 100 mT that the magnetization in the area delimited by the dotted lines in Fig. 5(a) becomes quasi uniformly aligned in the direction of H_0 , except on the edges of the antidots where the demagnetizing field is strong.

Therefore, in the following, we consider two very general states to describe the different magnetic configurations depending on the H_0 range. The magnetic configurations are referred as unsaturated

states or quasi-saturated states for values below or above 100 mT respectively. We do not refer to saturated states as the magnetization around the holes never aligns completely with the applied field even at 300 mT. The transition from unsaturated to quasi-saturated states appears at 110 mT for the parameters used in our simulations. Nevertheless, this value of transition field can be lower for perfect geometries such as squares or circles or if the magnetic parameters in the impacted volume are closer from the nominal values. It can also be higher if the impacted volume spreads on a lateral length larger than 210 nm. Then, the local geometrical and chemical variations most probably induce variations of the transition field across the sample. We assume that this is the origin of the strong red contrast observed experimentally in the FMR spectrum between 50 mT and 150 mT on a large frequency range. Such contrast means a strong averaged microwave absorption by the antidot lattice that we attribute to multiple absorption modes associated to the large transition regime.

This is the author's peer reviewed, accepted manuscript. However, the online version of record will be different from this version once it has been copyedited and typeset.
PLEASE CITE THIS ARTICLE AS DOI: 10.1063/1.50085623

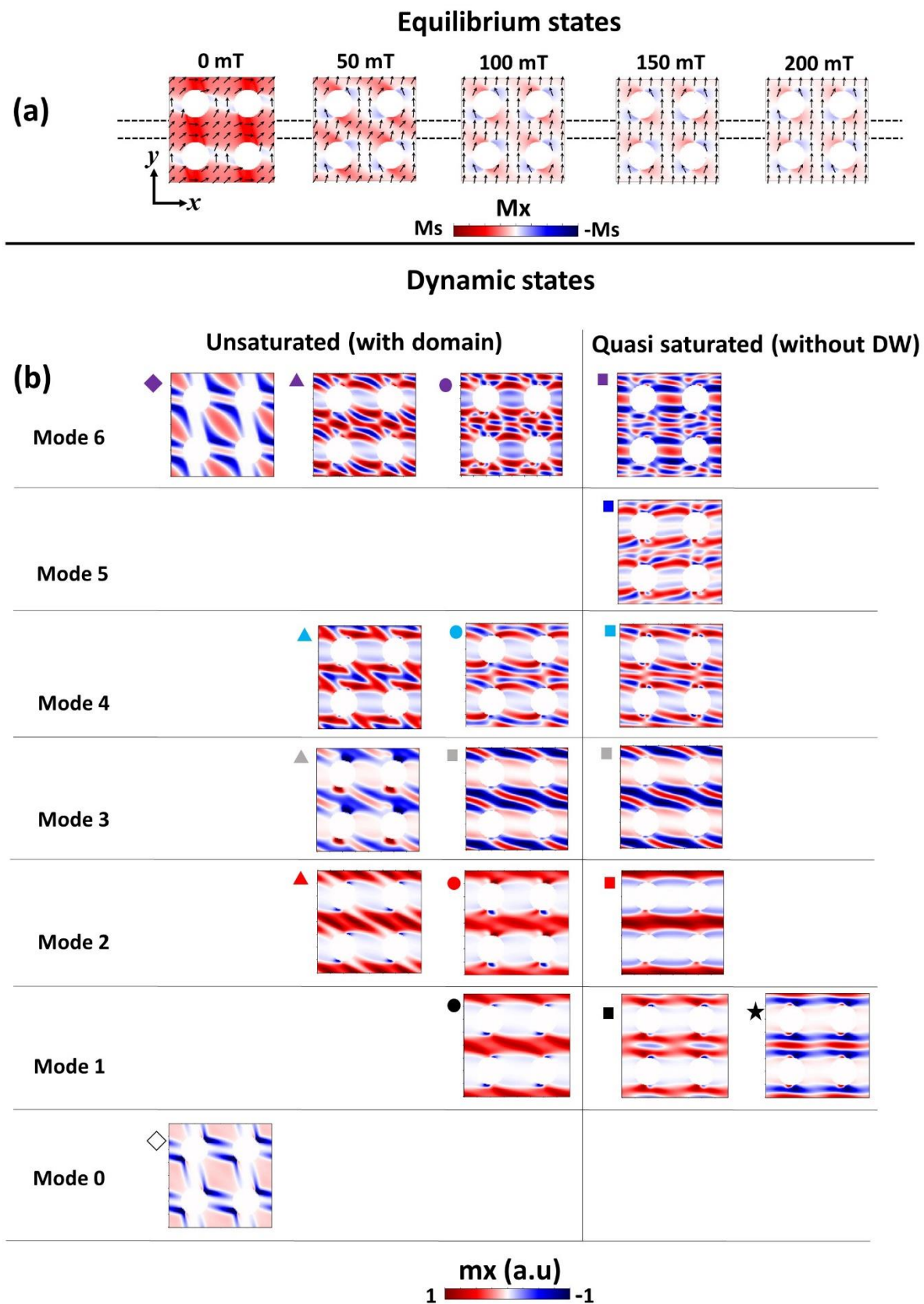


FIG. 5. (a) Equilibrium magnetic configuration for different values of H_0 . (b) Evolution of the spatial profile (m_x component) of the different modes as a function of the equilibrium state. The color and symbols are the same as in Fig. 3.

Now we turn to the study of the spatial profile of the spin waves modes. To define a mode we applied the following convention. Each main peak in the FFT spectra calculated at different values of H_0 corresponds to a mode. Each mode is attributed a color. The same color is given for the peaks that seem to follow the same experimental $f(H_0)$ dependence in Fig. 3. Now, each peak of a given mode is attributed a shape that depends on its spatial profile, thus the same shape at different values of H_0 means the same spatial profile.

The spatial profiles of the simulated modes are shown in Fig. 5(b). The main result is that each mode shows a strong variation as a function of H_0 . It is especially pronounced as long as the quasi-saturated state is not reached. Such result can be easily understood regarding the evolution of the equilibrium magnetization. As a general statement, magnetization precession appears mainly in the areas where the magnetization can couple to h_{rf} (i.e, the area where $m_y \neq 0$). Then, at zero field, spin waves will be strongly spatially localized in the 45° domain at the center of the unit cell and between horizontal antidots, as observed for the modes 0 and 6 (white and violet diamonds). On the contrary, in the quasi-saturated states, extended modes can spread over the x direction because the magnetization tends to be uniformly aligned between vertical antidots. Such extended modes, as the ones shown at 150 mT in Fig. 5(b) and for field values above, have been reported by others⁸⁰. At 50 mT, confined (mode 2) and extended (modes 3, 4 and 6) modes are both observed. It is interesting to observe extended modes in such unsaturated state but this can be explained by the fact that every part of the sample shows a non-null M_y component allowing a coupling with the RF field. However, their spatial profiles are quite complex and still influenced by the presence of the domain at the center of the unit cell as shown for the mode 4 for example.

V. Conclusion

In summary, we have investigated the FMR spectrum in a Heusler-based antidot lattice nanostructured by FIB technique. Only few magnonics studies have been performed with such materials whereas Co_2MnSi alloy is very promising for applications. Our results emphasize the necessity to take into account both the geometrical and chemical variations induced by Ga^+ milling to qualitatively and quantitatively describe the spin waves spectrum of a Co_2MnSi magnonic crystal in a large field range including unsaturated and quasi-saturated magnetic configurations. Many studies generally neglect this point, which is a prerequisite for proper design of devices.

The simple model proposed in our work is in favour of a very strong decrease of the magnetic parameters of the Co_2MnSi due to Ga^+ milling but without reaching a full paramagnetic state of the alloy. However, further studies are required to get a full in

depth understanding of the magnetic modifications induced by such process. We found that the strong decrease of magnetic parameters nearby the antidots is at the origin of a high frequency spin wave mode in the MC. We also demonstrated that the frequencies of other spin waves modes depend on the shape of the antidots and on the magnetic parameters in the impacted volume. Therefore, we assumed that small local geometrical and chemical variations must have an important contribution to the large the resonance peaks linewidths measured experimentally. For practical microwave applications requiring well-defined microwave absorption frequencies, further strategies must be developed to avoid such inhomogeneities when using Ga^+ FIB milling.

ACKNOWLEDGMENTS

We thank A. Claverie from the CEMES lab for SRIM simulations and fruitful discussions about the interactions of Ga^+ ions with the CMS alloy. This work was performed using HPC resources from CALMIP (Grant 2021-p1554).

DATA AVAILABILITY

The data that support the findings of this study are available from the corresponding author upon reasonable request.

VI. References.

- ¹ A.V. Chumak, A.A. Serga, and B. Hillebrands, J. Phys. D: Appl. Phys. **50**, 244001 (2017).
- ² Á. Papp, W. Porod, and G. Csaba, Nat Commun **12**, 6422 (2021).
- ³ A.V. Chumak, T. Neumann, A.A. Serga, B. Hillebrands, and M.P. Kostylev, J. Phys. D: Appl. Phys. **42**, 205005 (2009).
- ⁴ J. Topp, D. Heitmann, M.P. Kostylev, and D. Grundler, Phys. Rev. Lett. **104**, 207205 (2010).
- ⁵ J. Ding, M. Kostylev, and A.O. Adeyeye, Appl. Phys. Lett. **100**, 073114 (2012).
- ⁶ A. Haldar and A.O. Adeyeye, Journal of Applied Physics **128**, 240902 (2020).
- ⁷ H. Merbouche, I. Boventer, V. Haspot, S. Fusil, V. Garcia, D. Gouéré, C. Carrétéro, A. Vecchiola, R. Lebrun, P. Bortolotti, L. Vila, M. Bibes, A. Barthélémy, and A. Anane, ACS Nano **15**, 9775 (2021).
- ⁸ P.J. Brown, K.U. Neumann, P.J. Webster, and K.R.A. Ziebeck, J. Phys.: Condens. Matter **12**, 1827 (2000).
- ⁹ C. Guillemard, S. Petit-Watelot, L. Pasquier, D. Pierre, J. Ghanbaja, J.-C. Rojas-Sánchez, A.

This is the author's peer reviewed, accepted manuscript. However, the online version of record will be different from this version once it has been copyedited and typeset.
PLEASE CITE THIS ARTICLE AS DOI: 10.1063/5.0085623

- Bataille, J. Rault, P. Le Fèvre, F. Bertran, and S. Andrieu, *Phys. Rev. Applied* **11**, 064009 (2019).
- ¹⁰ T. Stücker, C. Liu, H. Yu, F. Heimbach, J. Chen, J. Hu, S. Tu, Md.S. Alam, J. Zhang, Y. Zhang, I.L. Farrell, C. Emeny, S. Granville, Z.-M. Liao, D. Yu, and W. Zhao, *Journal of Magnetism and Magnetic Materials* **450**, 13 (2018).
- ¹¹ T. Sebastian, Y. Ohdaira, T. Kubota, P. Pirro, T. Brächer, K. Vogt, A.A. Serga, H. Naganuma, M. Oogane, Y. Ando, and B. Hillebrands, *Appl. Phys. Lett.* **100**, 112402 (2012).
- ¹² I. Abdallah, B. Pradines, N. Ratel-Ramond, G. BenAssayag, R. Arras, L. Calmels, J.F. Bobo, E. Snoeck, and N. Biziere, *J. Phys. D: Appl. Phys.* **50**, 035003 (2017).
- ¹³ I. Abdallah, N. Ratel-Ramond, C. Magen, B. Pecassou, R. Cours, A. Arnoult, M. Respaud, J.F. Bobo, G. BenAssayag, E. Snoeck, and N. Biziere, *Mater. Res. Express* **3**, 046101 (2016).
- ¹⁴ R. Zivieri, S. Tacchi, F. Montoncello, L. Giovannini, F. Nizzoli, M. Madami, G. Gubbiotti, G. Carlotti, S. Neusser, G. Duerr, and D. Grundler, *Phys. Rev. B* **85**, 012403 (2012).
- ¹⁵ M. Krawczyk and H. Puszkarski, *Phys. Rev. B* **77**, 054437 (2008).
- ¹⁶ T. Kubota, S. Tsunegi, M. Oogane, S. Mizukami, T. Miyazaki, H. Naganuma, and Y. Ando, *Appl. Phys. Lett.* **94**, 122504 (2009).
- ¹⁷ J. Schmalhorst, A. Thomas, S. Kämmerer, O. Schebaum, D. Ebke, M.D. Sacher, G. Reiss, A. Hütten, A. Turchanin, A. Götzhäuser, and E. Arenholz, *Phys. Rev. B* **75**, 014403 (2007).
- ¹⁸ S. Andrieu, A. Neggache, T. Hauet, T. Devolder, A. Hallal, M. Chshiev, A.M. Bataille, P. Le Fèvre, and F. Bertran, *Phys. Rev. B* **93**, 094417 (2016).
- ¹⁹ M. Jourdan, J. Minár, J. Braun, A. Kronenberg, S. Chadov, B. Balke, A. Gloskovskii, M. Kolbe, H.J. Elmers, G. Schönhense, H. Ebert, C. Felser, and M. Kläui, *Nat Commun* **5**, 3974 (2014).
- ²⁰ C. de Melo, C. Guillemard, A.M. Friedel, V. Palin, J.C. Rojas-Sánchez, S. Petit-Watelot, and S. Andrieu, *Applied Materials Today* **25**, 101174 (2021).
- ²¹ C. Guillemard, W. Zhang, G. Malinowski, C. de Melo, J. Gorchon, S. Petit-Watelot, J. Ghanbaja, S. Mangin, P. Le Fèvre, F. Bertran, and S. Andrieu, *Advanced Materials* **32**, 1908357 (2020).
- ²² A.V. Chumak, V.I. Vasyuchka, A.A. Serga, and B. Hillebrands, *Nature Physics* **11**, 453 (2015).
- ²³ V. Vlaminck and M. Bailleul, *Science* **322**, 410 (2008).
- ²⁴ V.E. Demidov, S. Urazhdin, A. Anane, V. Cros, and S.O. Demokritov, *Journal of Applied Physics* **127**, 170901 (2020).
- ²⁵ T. Stücker, C. Liu, T. Liu, H. Yu, F. Heimbach, J. Chen, J. Hu, S. Tu, Y. Zhang, S. Granville, M. Wu, Z.-M. Liao, D. Yu, and W. Zhao, *Phys. Rev. B* **96**, 144430 (2017).
- ²⁶ S. Wang, J. Ding, X. Guan, M.B. Jungfleisch, Z. Zhang, X. Wang, W. Gu, Y. Zhu, J.E. Pearson, X. Cheng, A. Hoffmann, and X. Miao, *Appl. Phys. Lett.* **113**, 232404 (2018).
- ²⁷ T. Sebastian, T. Brächer, P. Pirro, A.A. Serga, B. Hillebrands, T. Kubota, H. Naganuma, M. Oogane, and Y. Ando, *Phys. Rev. Lett.* **110**, 067201 (2013).
- ²⁸ P. Pirro, T. Sebastian, T. Brächer, A.A. Serga, T. Kubota, H. Naganuma, M. Oogane, Y. Ando, and B. Hillebrands, *Phys. Rev. Lett.* **113**, 227601 (2014).
- ²⁹ S. Mallick, S. Mondal, T. Seki, S. Sahoo, T. Forrest, F. Maccherozzi, Z. Wen, S. Barman, A. Barman, K. Takanashi, and S. Bedanta, *Phys. Rev. Applied* **12**, 014043 (2019).
- ³⁰ M. Langer, K. Wagner, T. Sebastian, R. Hübner, J. Grenzer, Y. Wang, T. Kubota, T. Schneider, S. Stienen, K. Lenz, H. Schultheiß, J. Lindner, K. Takanashi, R.E. Arias, and J. Fassbender, *Appl. Phys. Lett.* **108**, 102402 (2016).
- ³¹ Z. Lazcano-Ortiz, C.L. Ordóñez-Romero, J.L. Domínguez-Juárez, G. Monsivais, R. Quintero-Torres, D. Matatagui, J.R. Fragoso-Mora, N. Qureshi, and O. Kolokoltsev, *Magnetochemistry* **7**, 155 (2021).
- ³² R. Mandal, P. Laha, K. Das, S. Saha, S. Barman, A.K. Raychaudhuri, and A. Barman, *Appl. Phys. Lett.* **103**, 262410 (2013).
- ³³ M. Zelent, N. Tahir, R. Gieniusz, J.W. Kłos, T. Wojciechowski, U. Guzowska, A. Maziewski, J. Ding, A.O. Adeyeye, and M. Krawczyk, *J. Phys. D: Appl. Phys.* **50**, 185003 (2017).
- ³⁴ J.W. Kłos, D. Kumar, M. Krawczyk, and A. Barman, *Sci Rep* **3**, 2444 (2013).
- ³⁵ G. Venkat, N. Kumar, and A. Prabhakar, *IEEE Transactions on Magnetics* **50**, 1 (2014).
- ³⁶ A.V. Chumak, A.A. Serga, B. Hillebrands, and M.P. Kostylev, *Appl. Phys. Lett.* **93**, 022508 (2008).
- ³⁷ A.V. Chumak, P. Pirro, A.A. Serga, M.P. Kostylev, R.L. Stamps, H. Schultheiss, K. Vogt, S.J.

This is the author's peer reviewed, accepted manuscript. However, the online version of record will be different from this version once it has been copyedited and typeset.
PLEASE CITE THIS ARTICLE AS DOI: 10.1063/1.50085623

- Hermsdoerfer, B. Laegel, P.A. Beck, and B. Hillebrands, *Appl. Phys. Lett.* **95**, 262508 (2009).
- ³⁸ S. Choudhury, S. Saha, R. Mandal, S. Barman, Y. Otani, and A. Barman, *ACS Appl. Mater. Interfaces* **8**, 18339 (2016).
- ³⁹ F.S. Ma, H.S. Lim, Z.K. Wang, S.N. Piramanayagam, S.C. Ng, and M.H. Kuok, *Appl. Phys. Lett.* **98**, 153107 (2011).
- ⁴⁰ B. Obry, P. Pirro, T. Brächer, A.V. Chumak, J. Osten, F. Ciubotaru, A.A. Serga, J. Fassbender, and B. Hillebrands, *Appl. Phys. Lett.* **102**, 202403 (2013).
- ⁴¹ L. Torres, L. Lopez-Diaz, and O. Alejos, *Journal of Applied Physics* **87**, 5645 (2000).
- ⁴² S.K. Abbas, M. Saleem, S. Naseem, S. Riaz, and S. Atiq, *Materials Letters* **271**, 127852 (2020).
- ⁴³ Q. Wang, Z. Zhong, L. Jin, X. Tang, F. Bai, H. Zhang, and G.S.D. Beach, *Journal of Magnetism and Magnetic Materials* **340**, 23 (2013).
- ⁴⁴ E.K. Semenova and D.V. Berkov, *Journal of Applied Physics* **114**, 013905 (2013).
- ⁴⁵ P.J. Metaxas, M. Sushruth, R.A. Begley, J. Ding, R.C. Woodward, I.S. Maksymov, M. Albert, W. Wang, H. Fangohr, A.O. Adeyeye, and M. Kostylev, *Appl. Phys. Lett.* **106**, 232406 (2015).
- ⁴⁶ R. Mandal, S. Barman, S. Saha, Y. Otani, and A. Barman, *Journal of Applied Physics* **118**, 053910 (2015).
- ⁴⁷ G. Gubbiotti, F. Montoncello, S. Tacchi, M. Madami, G. Carlotti, L. Giovannini, J. Ding, and A.O. Adeyeye, *Appl. Phys. Lett.* **106**, 262406 (2015).
- ⁴⁸ H. Ulrichs, B. Lenk, and M. Münzenberg, *Appl. Phys. Lett.* **97**, 092506 (2010).
- ⁴⁹ S. Neusser, B. Botters, M. Becherer, D. Schmitt-Landsiedel, and D. Grundler, *Appl. Phys. Lett.* **93**, 122501 (2008).
- ⁵⁰ N. Porwal, A. De, S. Mondal, K. Dutta, S. Choudhury, J. Sinha, A. Barman, and P.K. Datta, *Sci Rep* **9**, 12138 (2019).
- ⁵¹ S. Neusser, G. Duerr, S. Tacchi, M. Madami, M.L. Sokolovskyy, G. Gubbiotti, M. Krawczyk, and D. Grundler, *Phys. Rev. B* **84**, 094454 (2011).
- ⁵² S. Martens, O. Albrecht, K. Nielsch, and D. Görlitz, *Journal of Applied Physics* **105**, 07C113 (2009).
- ⁵³ *Amorphization Induced by Focused Ion Beam Milling in Metallic and Electronic Materials | Microscopy and Microanalysis | Cambridge Core* (n.d.).
- ⁵⁴ Y. Xiao, J. Wehrs, H. Ma, T. Al-Samman, S. Korte-Kerzel, M. Göken, J. Michler, R. Spolenak, and J.M. Wheeler, *Scripta Materialia* **127**, 191 (2017).
- ⁵⁵ D. Kiener, C. Motz, M. Rester, M. Jenko, and G. Dehm, *Materials Science and Engineering: A* **459**, 262 (2007).
- ⁵⁶ E.I. Preiß, B. Merle, Y. Xiao, F. Gannott, J.P. Liebig, J.M. Wheeler, and M. Göken, *Journal of Materials Research* **36**, 2505 (2021).
- ⁵⁷ J. Liu, R. Niu, J. Gu, M. Cabral, M. Song, and X. Liao, *Sci Rep* **10**, 10324 (2020).
- ⁵⁸ F. Albertini, L. Nasi, F. Casoli, S. Fabbri, P. Luches, G.C. Gazzadi, A. di Bona, P. Vavassori, S. Valeri, and S.F. Contri, *Journal of Applied Physics* **104**, 053907 (2008).
- ⁵⁹ I. Sveklo, P. Mazalski, J. Jaworowicz, J.P. Jamet, N. Vernier, A. Mougín, J. Ferré, M. Kisielewski, V. Zablotskii, E. Bourhis, J. Gierak, K. Postava, J. Fassbender, J. Kanak, and A. Maziewski, *Acta Phys. Pol. A* **133**, 1215 (2018).
- ⁶⁰ R. Mandal, S. Saha, D. Kumar, S. Barman, S. Pal, K. Das, A.K. Raychaudhuri, Y. Fukuma, Y. Otani, and A. Barman, *ACS Nano* **6**, 3397 (2012).
- ⁶¹ J. Hamrle, S. Blomeier, O. Gaier, B. Hillebrands, H. Schneider, G. Jakob, B. Reuscher, A. Brodyanski, M. Kopnarski, K. Postava, and C. Felser, *J. Phys. D: Appl. Phys.* **40**, 1558 (2007).
- ⁶² G. Ortiz, A. Garcia, J.B. Youssef, N. Biziere, F. Boust, J.-F. Bobo, E. Snoeck, and N. Vukadinovic, *IEEE Transactions on Magnetics* **49**, 1037 (2013).
- ⁶³ C. Guillemard, S. Petit-Watelot, T. Devolder, L. Pasquier, P. Boulet, S. Migot, J. Ghanbaja, F. Bertran, and S. Andrieu, *Journal of Applied Physics* **128**, 241102 (2020).
- ⁶⁴ S. Pan, S. Mondal, M. Zelent, R. Szwiercz, S. Pal, O. Hellwig, M. Krawczyk, and A. Barman, *Phys. Rev. B* **101**, 014403 (2020).
- ⁶⁵ A. Vansteenkiste, J. Leliaert, M. Dvornik, M. Helsen, F. Garcia-Sanchez, and B. Van Waeyenberge, *AIP Advances* **4**, 107133 (2014).
- ⁶⁶ D. Kumar, O. Dmytriiev, S. Ponraj, and A. Barman, *J. Phys. D: Appl. Phys.* **45**, 015001 (2012).
- ⁶⁷ M. Zelent, N. Tahir, R. Gieniusz, J.W. Kłos, T. Wojciechowski, U. Guzowska, A. Maziewski, J. Ding, A.O. Adeyeye, and M. Krawczyk, *J. Phys. D: Appl. Phys.* **50**, 185003 (2017).
- ⁶⁸ S. Tacchi, P. Gruszecki, M. Madami, G. Carlotti, J.W. Kłos, M. Krawczyk, A. Adeyeye, and G. Gubbiotti, *Sci Rep* **5**, 10367 (2015).
- ⁶⁹ N. Vladov, J. Segal, and S. Ratchev, *Journal of Vacuum Science & Technology B, Nanotechnology and Microelectronics:*

This is the author's peer reviewed, accepted manuscript. However, the online version of record will be different from this version once it has been copyedited and typeset.
PLEASE CITE THIS ARTICLE AS DOI: 10.1063/1.50085623

Materials, Processing, Measurement, and Phenomena **33**, 041803 (2015).

⁷⁰ J.F. Ziegler, M.D. Ziegler, and J.P. Biersack, Nuclear Instruments and Methods in Physics Research Section B: Beam Interactions with Materials and Atoms **268**, 1818 (2010).

⁷¹ S. Pal, J.W. Klos, K. Das, O. Hellwig, P. Gruszecki, M. Krawczyk, and A. Barman, Appl. Phys. Lett. **105**, 162408 (2014).

⁷² J.M. Shaw, S.E. Russek, T. Thomson, M.J. Donahue, B.D. Terris, O. Hellwig, E. Dobisz, and M.L. Schneider, Phys. Rev. B **78**, 024414 (2008).

⁷³ R. Hyndman, P. Warin, J. Gierak, J. Ferré, J.N. Chapman, J.P. Jamet, V. Mathet, and C. Chappert, Journal of Applied Physics **90**, 3843 (2001).

⁷⁴ M. Urbánek, L. Flajšman, V. Křižáková, J. Gloss, M. Horký, M. Schmid, and P. Varga, APL Materials **6**, 060701 (2018).

⁷⁵ I. Utke, P. Hoffmann, and J. Melngailis, J. Vac. Sci. Technol. B **26**, 1197 (2008).

⁷⁶ C. Castán-Guerrero, J. Herrero-Albillos, J. Bartolomé, F. Bartolomé, L.A. Rodríguez, C. Magén, F. Kronast, P. Gawronski, O. Chubykalo-Fesenko, K.J. Merazzo, P. Vavassori, P. Strichovanec, J. Sesé, and L.M. García, Phys. Rev. B **89**, 144405 (2014).

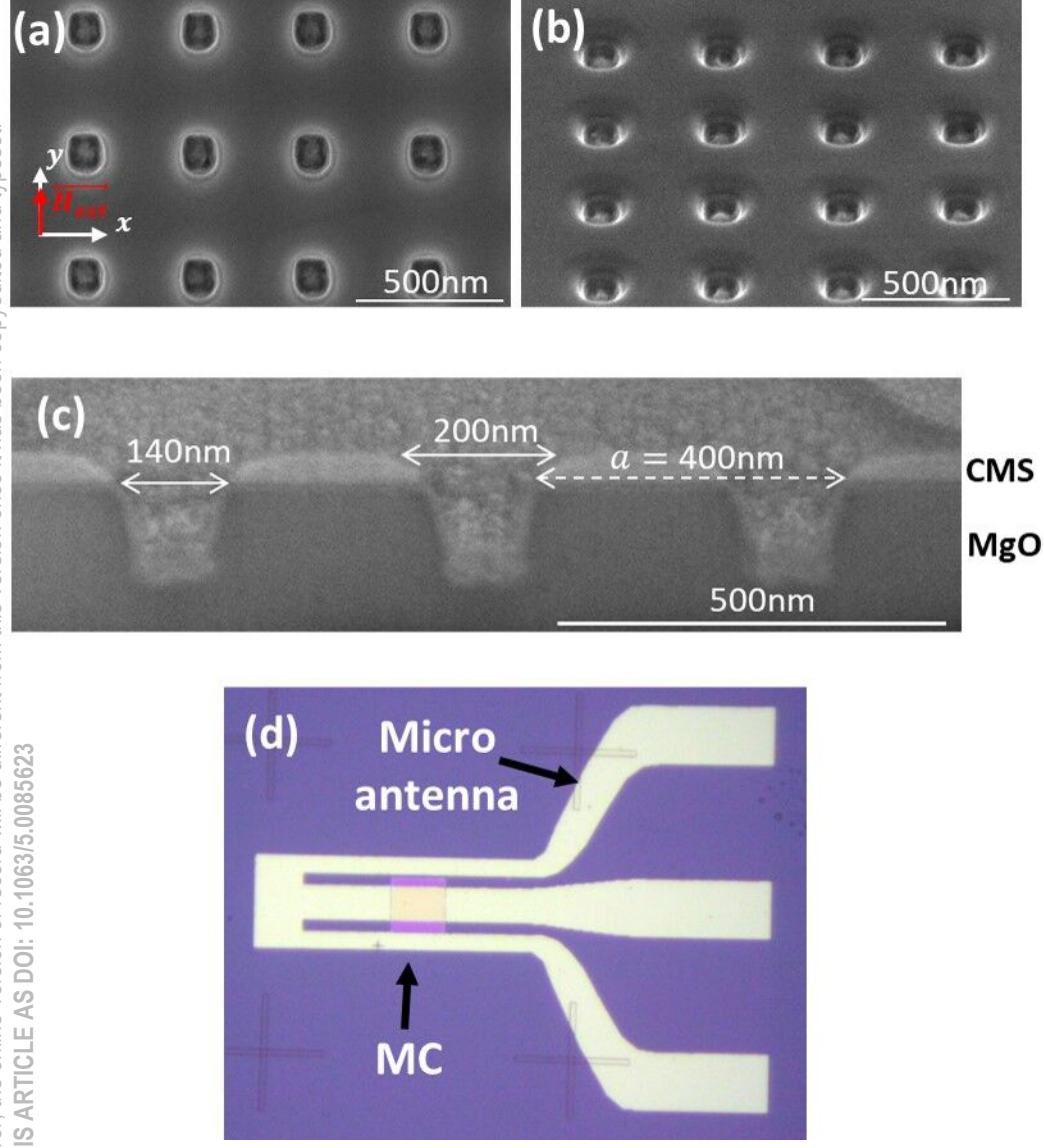
⁷⁷ L.A. Rodríguez, C. Magén, E. Snoeck, C. Gatel, C. Castán-Guerrero, J. Sesé, L.M. García, J. Herrero-Albillos, J. Bartolomé, F. Bartolomé, and M.R. Ibarra, Nanotechnology **25**, 385703 (2014).

⁷⁸ D.H.Y. Tse, S.J. Steinmuller, T. Trypiniotis, D. Anderson, G.A.C. Jones, J.A.C. Bland, and C.H.W. Barnes, Phys. Rev. B **79**, 054426 (2009).

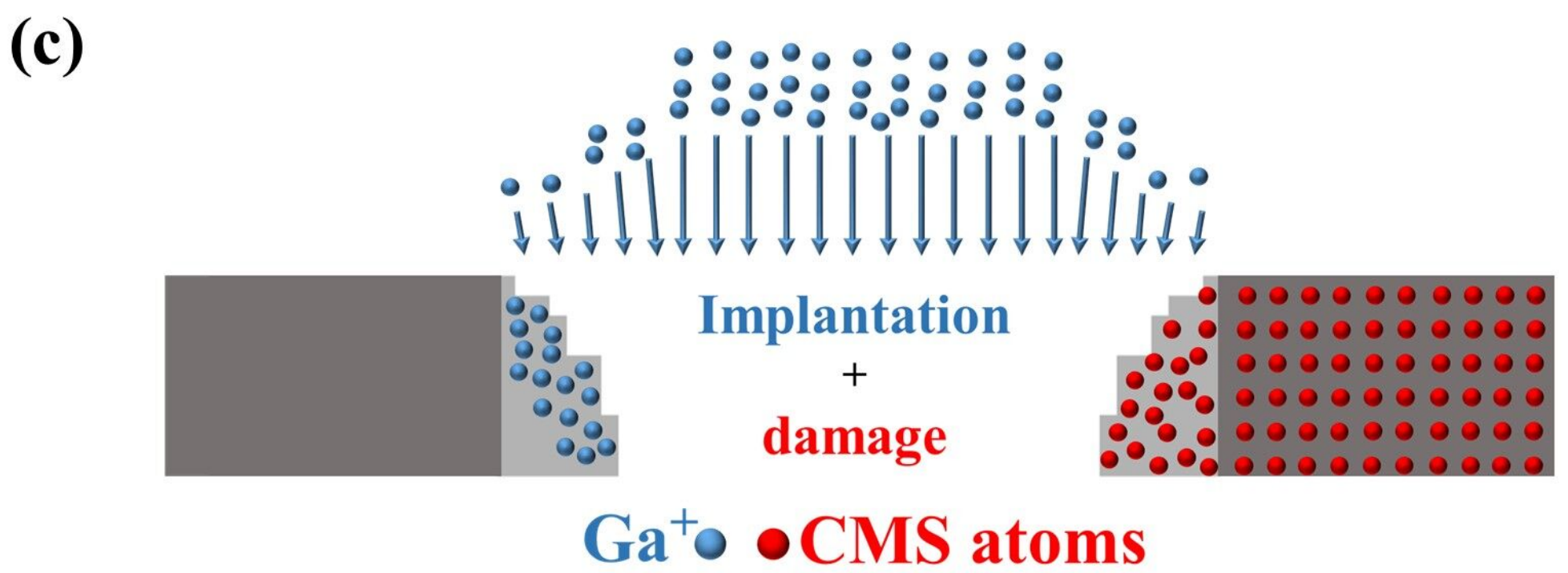
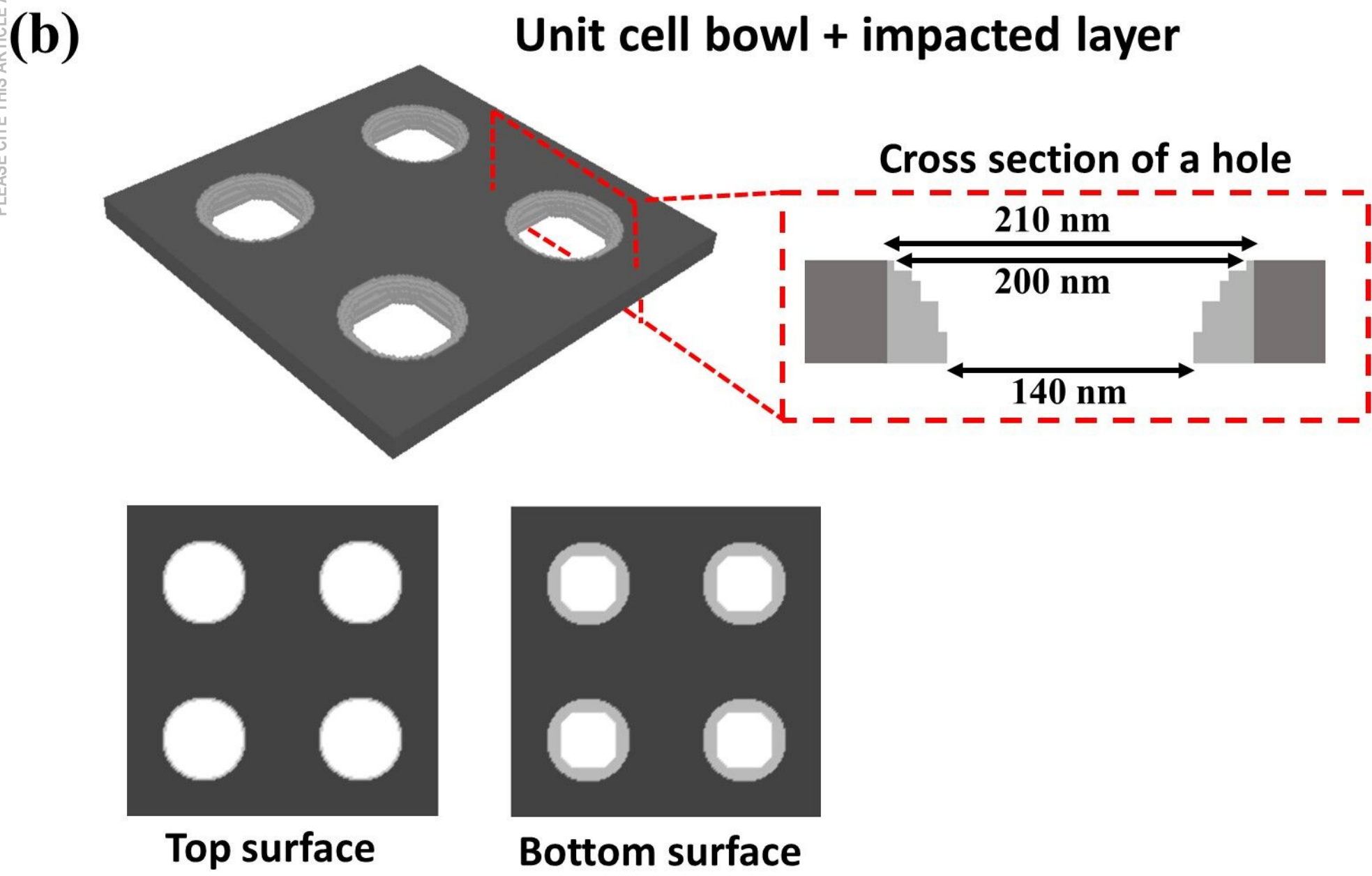
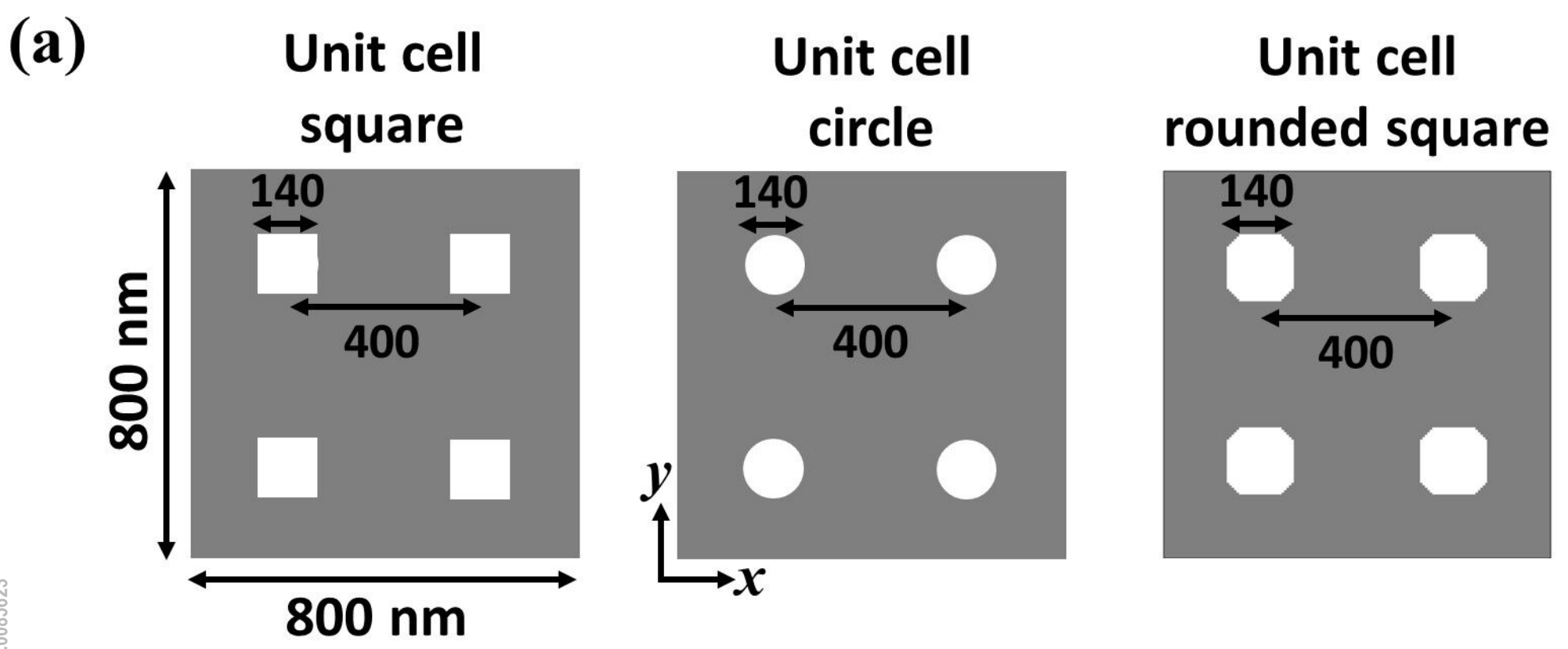
⁷⁹ R.D. McMichael and B.B. Maranville, Phys. Rev. B **74**, 024424 (2006).

⁸⁰ R. Zivieri, S. Tacchi, F. Montoncello, L. Giovannini, F. Nizzoli, M. Madami, G. Gubbiotti, G. Carlotti, S. Neusser, G. Duerr, and D. Grundler, Phys. Rev. B **85**, 012403 (2012).

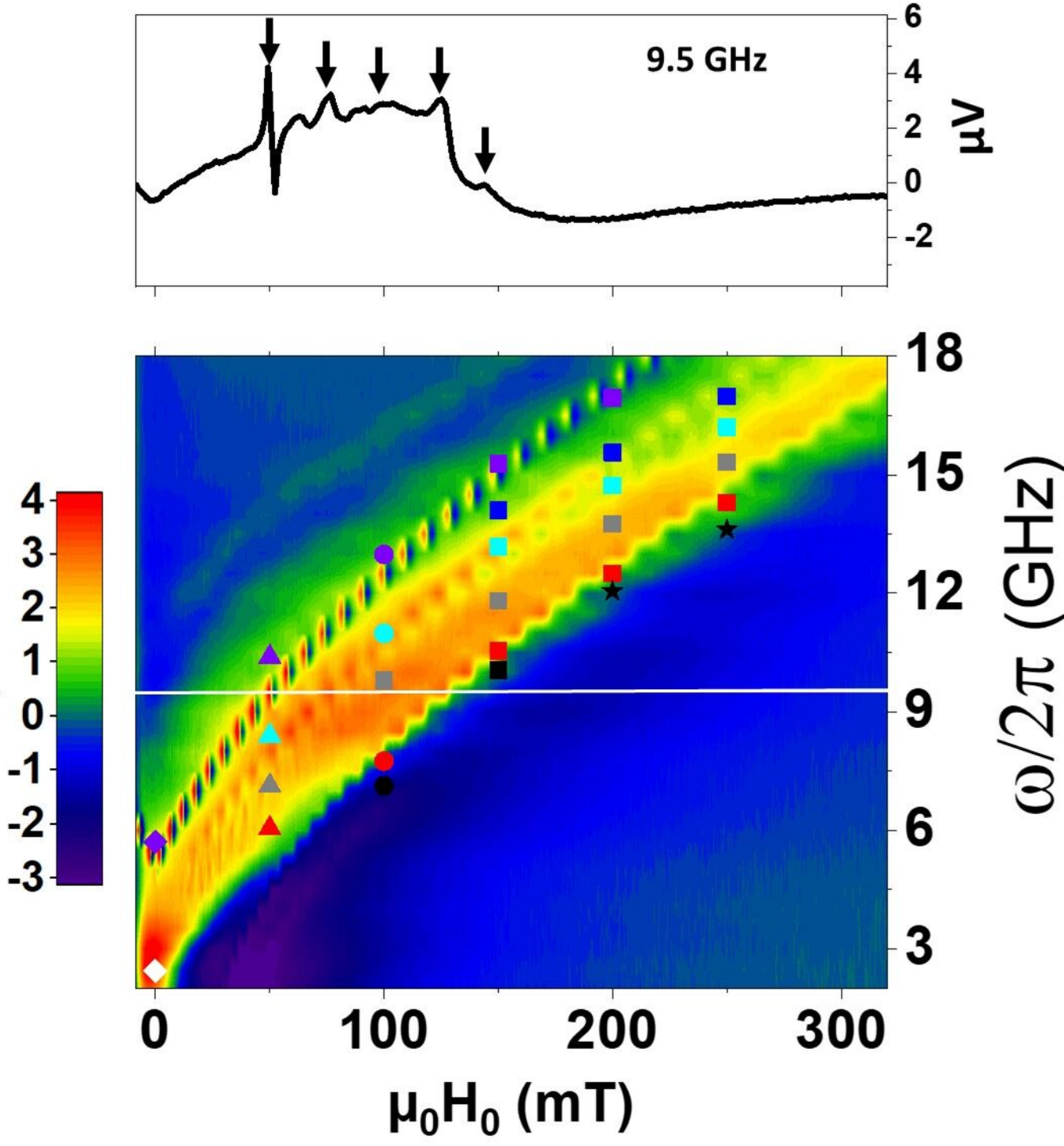
This is the author's peer reviewed, accepted manuscript. However, the online version of record will be different from this version once it has been copyedited and typeset.
PLEASE CITE THIS ARTICLE AS DOI: 10.1063/5.0085623



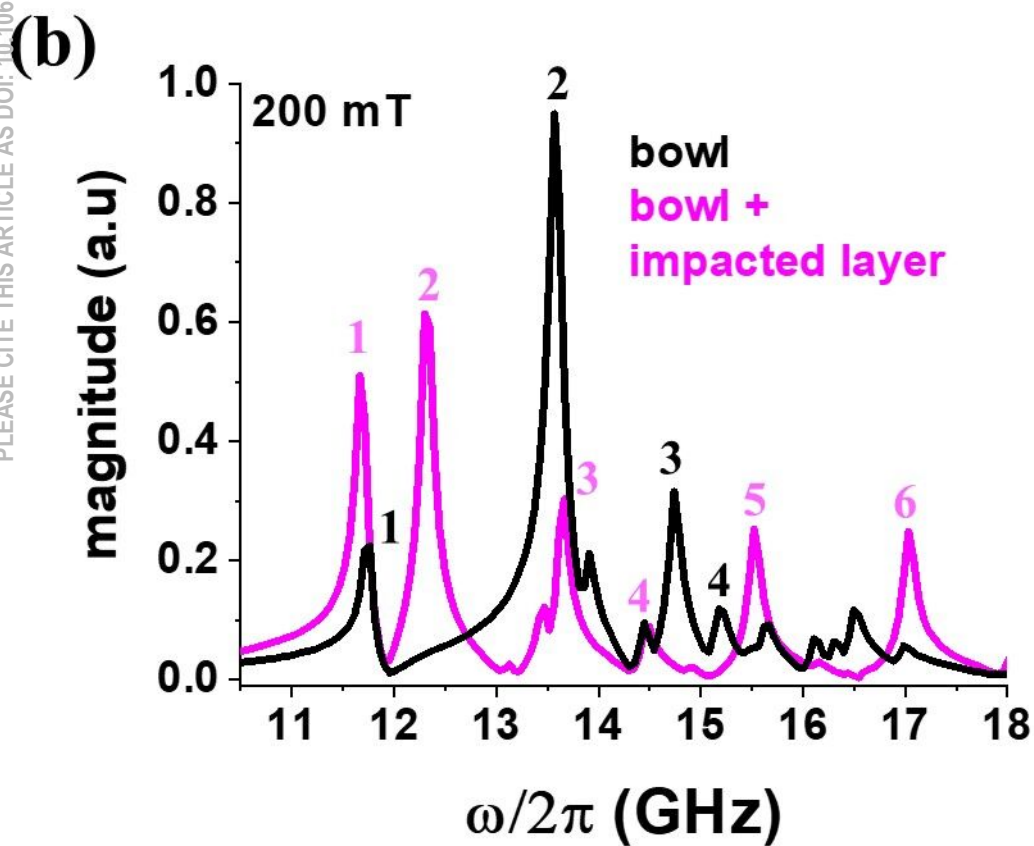
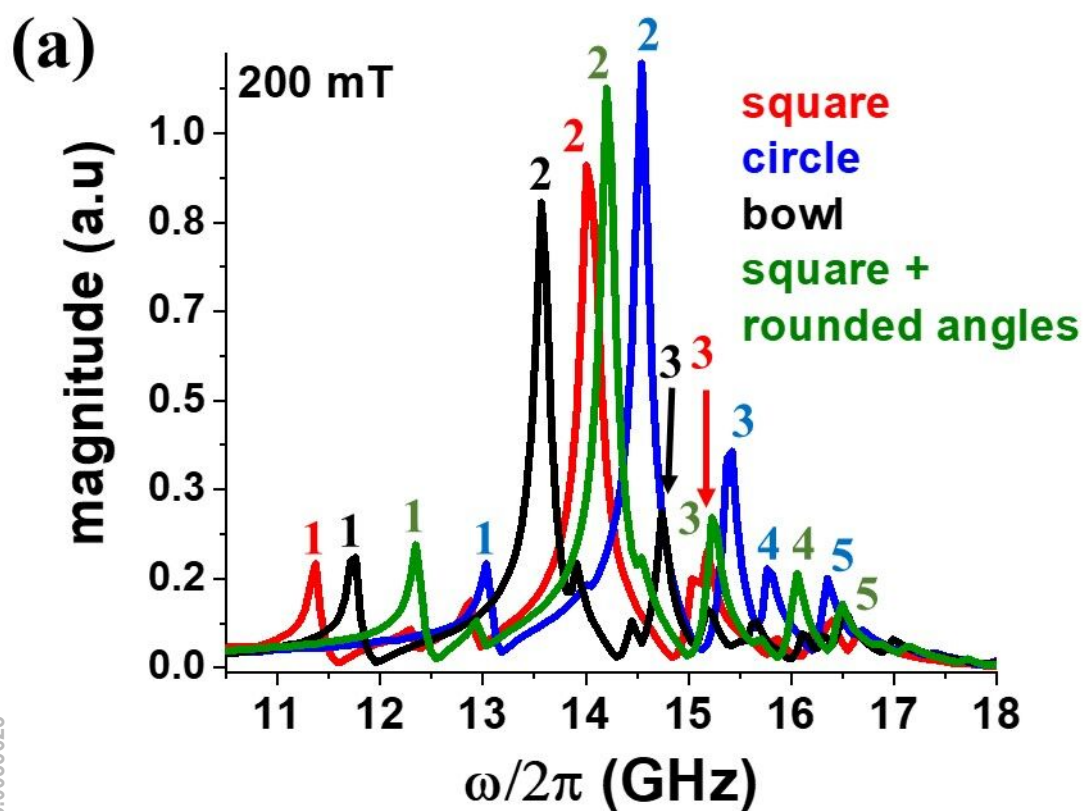
This is the author's peer reviewed, accepted manuscript. However, the online version of record will be different from this version once it has been copyedited and typeset.
PLEASE CITE THIS ARTICLE AS DOI: 10.1063/1.50085623



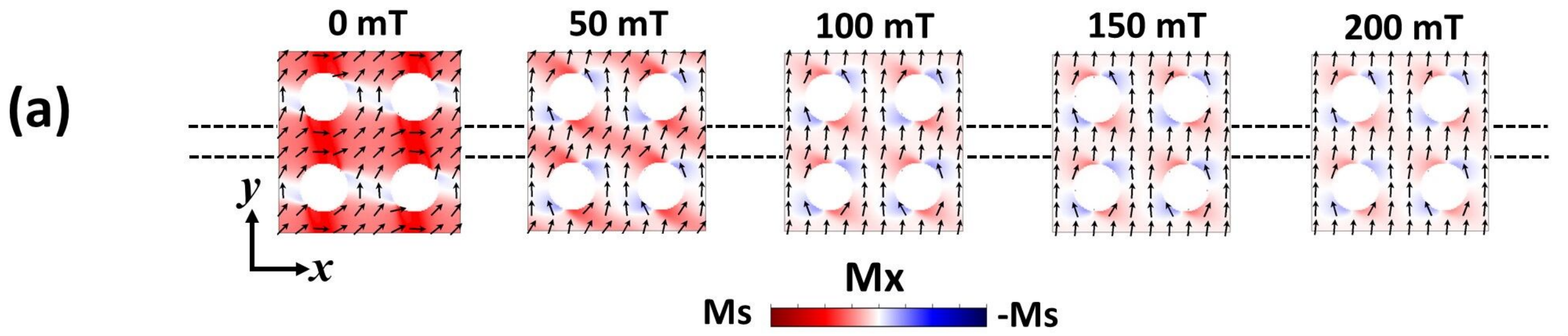
This is the author's peer reviewed, accepted manuscript. However, the online version of reports will be different from this version once it has been copyedited and typeset.
PLEASE CITE THIS ARTICLE AS DOI: 10.1063/1.50085623



This is the author's peer reviewed, accepted manuscript. However, the online version of record will be different from this version once it has been copyedited and typeset.
PLEASE CITE THIS ARTICLE AS DOI: 10.1063/5.0085623



Equilibrium states



Dynamic states

